Potential surfaces and dynamics of the $O(^3P)+H_2O(X\,^1A_1)\rightarrow OH(X\,^2\Pi)+OH(X\,^2\Pi)$ reaction

M. Braunstein,[a] R. Panfili, R. Shroll, and L. Bernstein
Spectral Sciences, Inc., Burlington, Massachusetts 01803

(Received 27 December 2004; accepted 24 February 2005; published online 9 May 2005)

We present global potential energy surfaces for the three lowest triplet states in $O(^3P)+H_2O(X\,^1A_1)$ collisions and present results of classical dynamics calculations on the $O(^3P)+H_2O(X\,^1A_1)\rightarrow OH(X\,^2\Pi)+OH(X\,^2\Pi)$ reaction using these surfaces. The surfaces are spline-based fits of ~20 000 fixed geometry *ab initio* calculations at the complete-active-space self-consistent field+second-order perturbation theory (CASSCF+MP2) level with a O(4*s*3*p*2*d*1*f*)/H(3*s*2*p*) one electron basis set. Computed rate constants compare well to measurements in the 1000–2500 K range using these surfaces. We also compute the total, rovibrationally resolved, and differential angular cross sections at fixed collision velocities from near threshold at ~4 km s^{-1} (16.9 kcal mol^{-1} collision energy) to 11 km s^{-1} (122.5 kcal mol^{-1} collision energy), and we compare these computed cross sections to available space-based and laboratory data. A major finding of the present work is that above ~40 kcal mol^{-1} collision energy rovibrationally excited $OH(X\,^2\Pi)$ products are a significant and perhaps dominant contributor to the observed 1–5 μ spectral emission from $O(^3P)+H_2O(X\,^1A_1)$ collisions. Another important result is that $OH(X\,^2\Pi)$ products are formed in two distinct rovibrational distributions. The "active" OH products are formed with the reagent O atom, and their rovibrational distributions are extremely hot. The remaining "spectator" OH is relatively rovibrationally cold. For the active OH, rotational energy is dominant at all collision velocities, but the opposite holds for the spectator OH. Summed over both OH products, below ~50 kcal mol^{-1} collision energy, vibration dominates the OH internal energy, and above ~50 kcal mol^{-1} rotation is greater than vibrational energy. As the collision energy increases, energy is diverted from vibration to mostly translational energy. We note that the present fitted surfaces can also be used to investigate direct collisional excitation of $H_2O(X\,^1A_1)$ by $O(^3P)$ and also $OH(X\,^2\Pi)+OH(X\,^2\Pi)$ collisions. © *2005 American Institute of Physics*.
[DOI: 10.1063/1.1893887]

I. INTRODUCTION

Collisions of $O(^3P)$ with $H_2O(X\,^1A_1)$ give rise to spectral radiation observed from the long wave infrared (~20–10 μ),[1–3] through the infrared (10-1 μ)[1–9] and up to the vacuum ultraviolet (~0.25 μ),[10–12] depending on the relative collision energy. These emissions are important to characterize because they can be a significant background noise source for telescopes mounted on spacecraft in low-Earth-orbit or LEO. In LEO (~300 km altitude and ~8 km s^{-1} relative atmospheric velocity), $O(^3P)$, which is the main component of the atmosphere at these altitudes, collides with $H_2O(X\,^1A_1)$ from outgassing spacecraft surfaces or from spacecraft engine exhaust.[4]

The mechanisms that give rise to the observed radiation in $O(^3P)+H_2O(X\,^1A_1)$ collisions remain elusive, however, because the rarefied conditions and large relative collision velocities necessary are difficult to achieve in the laboratory, and so experimental data remain sparse and difficult to interpret. Focusing on the 1–5 μ region, Bernstein *et al.*[7] have shown through analysis of space experiments and laboratory data that the observed radiation from $O(^3P)+H_2O(X\,^1A_1)$ collisions may be consistent with forming rovibrationally excited OH through hydrogen abstraction,

$$O(^3P)+H_2O(X\,^1A_1)\rightarrow OH(X\,^2\Pi)+OH(X\,^2\Pi),\qquad \Delta H=+16.9\ \text{kcal mol}^{-1}, \tag{1}$$

and/or forming rovibrationally excited H_2O through direct collisional excitation,

$$O(^3P)+H_2O[X\,^1A_1,(\nu_1\nu_2\nu_3,JK)]\rightarrow O(^3P)+H_2O[X\,^1A_1,(\nu_1'\nu_2'\nu_3',J'K')], \tag{2}$$

depending on the collision velocity. Other studies[6] have attributed all such radiation from 1–5 μ to reaction (2). It is particularly difficult to distinguish between Eqs. (1) and (2) in the 1–5 μ spectral region because spectral observations remain the main source of data and $OH(X\,^2\Pi)$ and $H_2O(X\,^1A_1)$ have highly overlapping spectral distributions in this region. Furthermore, since spectral observations are only sensitive to internally excited products, the magnitude and energy dependence of these observations minimize contributions from products formed with little internal excitation, products which may in fact carry most of the total reaction

[a]Electronic mail: matt@spectral.com

cross section and dynamical information. In addition, theoretical examination of the reactions (1) and (2) has been problematic because they involve computation of high-spin open shell wave functions which presents special difficulties for theory. There have been theoretical studies which used nonreactive $O(^3P)+H_2O(X\,^1A_1)$ potential surfaces to examine the collisional excitation channel [Eq. (2)].[13–16] Although these studies have had some success in explaining measurements in the 1–5 μ region, there remain major differences between these studies and measurements at certain collision velocities and significant differences between the theoretical results themselves.

Besides being important in LEO conditions, collisions of $O(^3P)+H_2O(X\,^1A_1)$ are also important in H_2/O_2 combustion chemistry.[17] The reverse of reaction (1) is an important step in such chemistry. In fact, the surfaces involved in reaction (1) are part of a family of triplet H_2O_2 surfaces leading to $H_2(X\,^1\Sigma_g^+)+O_2(X\,^3\Sigma_g^-)$ and $H(^2S)+OOH(X\,^2A')$, pathways critical in understanding such combustion chemistry. The potential surfaces involved in $O(^3P)+H_2O(X\,^1A_1)$ collisions have been probed recently using transition state photoelectron spectroscopy,[18,19] which has given information about the barrier height and other transition state properties for reaction (1). Instead of translational energy as in previous space and laboratory measurements, Ref. 20 used vibrational energy of deuterated H_2O reagents to overcome the large endothermicity of reaction (1),

$$O(^3P) + HOD(X\,^1A_1, 4_\nu OH) \rightarrow OH(X\,^2\Pi) + OD(X\,^2\Pi), \quad \Delta H = +16.9 \text{ kcal mol}^{-1}. \tag{3}$$

In these experiments, product internal state distributions were measured directly through laser-induced fluorescence, and therefore the usual ambiguities in interpreting the overlapping spectra of reactions (1) and (2) were removed. These measurements yield rich dynamical information on the surfaces involved in reaction (1).

For completeness, we note that collisions of $O(^3P)+H_2O(X\,^1A_1)$ at very large relative collision velocities can produce electronically excited $OH(A\,^2\Sigma^+)$,

$$O(^3P) + H_2O(X\,^1A_1) \rightarrow OH(A\,^2\Sigma^+) + OH(X\,^2\Pi), \quad \Delta H = +110.5 \text{ kcal mol}^{-1}, \tag{4}$$

which has been observed in space-based[11] and laboratory molecular beam measurements.[10] The electronically excited OH is apparently formed through high-lying conical intersections in the potential energy surfaces of the four-atom complex.[12] The surfaces involved in reactions (1) and (2) are part of a large manifold of electronic states which give rise to the products of reaction (4).

In this paper, we present global potential energy surfaces for the three lowest triplet adiabatic surfaces involved in $O(^3P)+H_2O(X\,^1A_1)$ collisions and present results for classical dynamics calculations on these surfaces. The main purpose of the paper is to investigate the role of reaction (1) in producing spectral radiation in the 1–5 μ region. By comparing to available measurements, we will assess the validity of these surfaces for further dynamical studies including reaction (2) in order to form a complete picture of $O(^3P)+H_2O(X\,^1A_1)$ collisions over a broad energy range. The present work is also of interest as a guide to the design and analysis of possible future hyperthermal O atom + H_2O beam measurements. In these experiments, it should be possible to measure the OH products and their internal state distributions directly, rather than through spectral emission, over a range of energies near 64 kcal mol^{-1} (~8 km s^{-1} relative collision velocity).[21]

The surfaces we report for $O(^3P)+H_2O(X\,^1A_1)$ are spline-based fits based on ~20 000 fixed geometry *ab initio* calculations at the complete-active-space self-consistent field +second-order perturbation theory (CASSCF+MP2) level with a O(4*s*3*p*2*d*1*f*)/H(3*s*2*p*) one electron basis set. The surfaces are used in quasiclassical trajectory (QCT) calculations to compute rate constants of reaction (1) as a function of temperature. The computed rate constants compare very well to available measurements. We also compute the total, rovibrationally resolved, and differential angular cross sections for reaction (1) with QCT on the fitted surfaces at fixed velocities from threshold at ~4 km s^{-1}–11 km s^{-1} relative collision velocity (122.5 kcal mol^{-1}). We compare the computed cross sections to available space-based and laboratory data. We also compute cross sections for reaction (3) and compare these results to results of Ref. 20 using the fitted surfaces.

A major finding of the present work is that the rovibrationally excited $OH(X\,^2\Pi)$ product from $O(^3P)+H_2O(X\,^1A_1)$ collisions are a significant and perhaps dominant contributor to 1–5 μ spectral emission above ~40 kcal mol^{-1} collision energy. This finding is in contrast to most interpretations of the experimental data which attribute this radiation to collisional excitation of $H_2O(X\,^1A_1)$ exclusively.[6] Another important result is that $OH(X\,^2\Pi)$ products of reaction (1) are formed in two distinct rovibrational distributions. The "active" OH products are formed with the reagent O atom, and their rovibrational distributions are extremely hot. The remaining "spectator" OH is relatively rovibrationally cold. Summed over both OH products, below ~50 kcal mol^{-1} collision energy, vibration dominates the OH internal energy. Above ~50 kcal mol^{-1}, rotation is greater than vibrational energy, but the total product energy fraction is mostly in translation. We note that the present surfaces can also be used to investigate collisional excitation of $H_2O(X\,^1A_1)$, reaction (2), or $OH(X\,^2\Pi)+OH(X\,^2\Pi)$ collisions, the reverse of reaction (1) but we leave such work for a separate study.

The methods used for the potential fit, the analytic representation of the fit, the fitted surface properties for all three triplet surfaces, and the QCT dynamics methods used are discussed in Sec. II. Section III presents the results of the QCT calculations and compares results to available experimental data. Section IV discusses possible future work.

II. METHODS

A. Potential surfaces

Collisions of $O(^3P)$ with $H_2O(X\,^1A_1)$ give rise to three electronic states which adiabatically lead to $OH(X\,^2\Pi)$

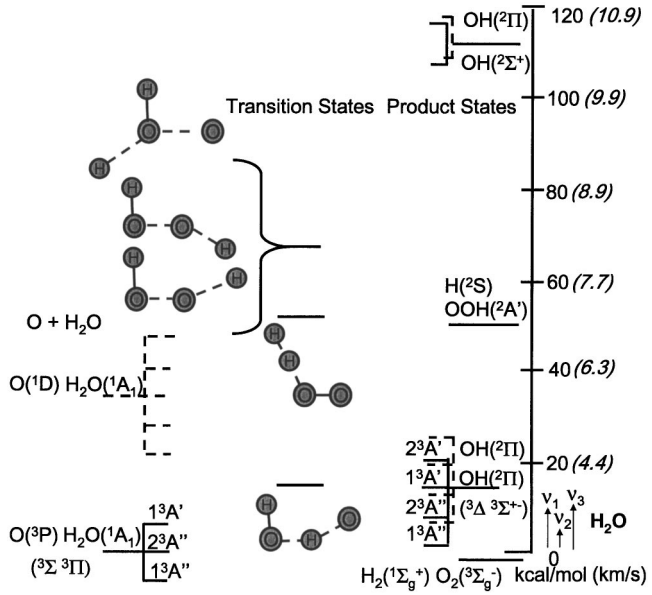

FIG. 1. Energy level diagram of low-lying triples (solid lines) and singlets (dashed lines) showing reagents, transition states, and products for $O+H_2O$ collisions. The transition state geometries and energy levels are for triplets based on the work of Ref. 17. The energy and corresponding relative collision velocities are shown in parentheses with respect to the $O(^3P)+H_2O(X\,^1A_1)$ asymptote at zero energy. The energies of the fundamental vibrational modes of H_2O are shown for reference. In the present study, we adiabatically follow the three lowest triplet states of $O(^3P)+H_2O(X\,^1A_1)$ to $OH(X\,^2\Pi)+OH(X\,^2\Pi)$.

$+OH(X\,^2\Pi)$. These three lowest triplet adiabatic states are the focus of the present study, and we label them "state 1," "state 2," and "state 3," where state 1 is the lowest energy state and state 3 is the highest. We fit these adiabatic states independently. The ΔH of the $O(^3P)+H_2O(^1A_1)\rightarrow OH(X\,^2\Pi)+OH(X\,^2\Pi)$ reaction is +16.9 kcal mol^{-1}. From rate constant measurements, the activation energy is $\sim$17.0 kcal mol^{-1} (Refs. 22 and 23) or a relative collision velocity of 4.1 km s^{-1}, which implies a very small energy barrier of $\sim$0.1 kcal mol^{-1}. We note that crossings of the three lowest triplet states with higher triplet states can lead to electronically excited $OH(A\,^2\Sigma^+)$ with an endothermicity of +110.5 kcal mol^{-1} (Ref. 12) but we do not consider such interactions here. Nor do we consider crossings with excited singlet oxygen $O(^1D)+H_2O(X\,^1A_1)$ states, which can also lead to $OH(X\,^2\Pi)+OH(X\,^2\Pi)$.[24] We further note that by symmetry there is a fourth triplet leading adiabatically to $OH(X\,^2\Pi)+OH(X\,^2\Pi)$ but this state must originate from electronically excited triplets of $O+H_2O$. Furthermore, $O(^3P)+H_2O(X\,^1A_1)$ reaction channels leading to $H_2(^1\Sigma_g^+)+O_2(^3\Sigma_g^-)$, $\Delta H=-1.6$ kcal mol^{-1}, and $H(^2S)+OOH(^2A')$, $\Delta H=+51.0$ kcal mol^{-1} are not addressed here. These channels go through high-lying transition states (60–70 kcal mol^{-1}) (Ref. 17) and should be accessible at hyperthermal energies. Fully global surfaces for triplet $O+H_2O$ should take these channels into account. A summary of the $O+H_2O$ reagent, transition states based on the work of Ref. 17, and product states is shown in Fig. 1. In the present study we follow the three lowest triplet states of $O(^3P)+H_2O(^1A_1)$ adiabatically to $OH(X\,^2\Pi)+OH(X\,^2\Pi)$ products.

The approach taken to fit the three lowest triplet adiabatic surfaces follows closely the work of Wu *et al.*[25] for the reaction $H+H_2O\rightarrow OH+H_2$ but with some modifications which we discuss below. For each triplet surface, we treat the full $(3N-6)=6$ dimensions by defining three "active" internal coordinates which most affect motion along the reaction path (bond breaking and forming) and three remaining "spectator" internal coordinates. The active coordinate potential is a three-dimensional spline determined from a large set of *ab initio* calculations spanning the range of active coordinate values. The spectator coordinate potential is determined for a fixed set of active coordinates at a geometry near the transition state of state 1. An approximation is made that the spectator coordinate potential does not vary much along the reaction pathway (changes in the active coordinates). A global analytic representation of a particular surface is defined as a sum of active and spectator parts. The global potential surface connects reagents to products smoothly and includes the proper symmetrization with respect to O-atom attack on either of the H_2O H atoms. The active potential spline coefficients, spectator potential parameters, and other parameters which determine the surface analytic representation are based on new *ab initio* calculations of the $O(^3P)+H_2O(^1A_1)$ potential at the CASSCF+MP2 level. The internal coordinates, analytic potential representation, *ab initio* calculations, and properties of the fitted surfaces are described below.

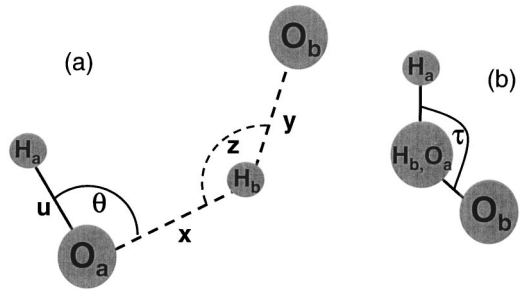

FIG. 2. Internal coordinates used in the description of the $O(^3P)+H_2O(X\,^1A_1)$ potential energy surfaces. Active coordinates (dashed lines) are the set $\{x,y,z\}$ and spectator coordinates (solid lines) are the set $\{u,\theta,\tau\}$. (a) illustrates the $\{x,y,z,u,\theta\}$ "in-plane" coordinates and (b) illustrates the "out-of-plane" τ coordinate looking along the O_a–H_b bond.

1. Internal coordinates

Figure 2 shows the internal coordinates used. The active coordinates are the set $\{x,y,z\}$ which most affect reaction going to OH products. The coordinate x is the OH bond of H_2O being broken, y is the OH bond being formed, and z is the angle formed between the breaking and forming bond, atoms O_a–H_b–O_b. The spectator coordinates are the set $\{u,\theta,\tau\}$, where u is the OH bond length of H_2O which is not attacked by the incoming O, θ is the H_a–O_a–H_b bond angle, and τ is the "out-of-plane" torsion angle defined as the angle between H_a and O_b when viewed along the O_a–H_b bond. The active coordinates have the range $\{x,0\rightarrow\infty,y,0\rightarrow\infty;z,0\rightarrow180°\}$, while the spectator coordinates have the range $\{u,0\rightarrow\infty;\theta,0\rightarrow360°;\tau,0\rightarrow180°\}$.

2. Analytic representation of the surfaces

We first define the "active+spectator" potential, V_{a+s}, as a sum of active V_a and spectator V_s parts,

$$V_{a+s}(x,y,z,u,\theta,\tau) = V_a(x,y,z)_{u_0,\theta_0,\tau} + V_s(u,\theta)_{x_0,y_0,z_0,\tau_0}, \quad (5)$$

The parameters $(x_0,y_0,z_0,u_0,\theta_0,\tau_0)$ are particular values of the internal coordinates defined further below. The active potential is further broken down into a weighted sum of two parts that depend on τ,

$$V_a = W(\tau)V_{\text{spline}}(x,y,z)_{u_0\vartheta_0,\tau=0} + [1 - W(\tau)]V_{\text{spline}}(x,y,z)_{u_0\vartheta_0,\tau=180°}. \quad (6)$$

The potential V_{spline} is defined as a three-dimensional (3D) spline interpolation[26] on a grid of calculated *ab initio* points in (x,y,z) described further below. Notice that the spline potential only depends on planar geometries of the $O+H_2O$ system and for purposes of the spline interpolation, z is considered to be continuous from 0 to 360°. $W(\tau)$ is a weighting function that weights the $\tau=0°$ and $\tau=180°$ V_{spline} values and provides an interpolation of the active potential for nonplanar geometries, $\tau \neq 0°$, 180° based on the planar V_{spline} values. $W(\tau)$ is defined

$$W(\tau) = \sum_{m=0}^{6} a_m \cos^m \tau, \quad (7)$$

where the parameters $\{a_m\}$ are parameters determined from a fit of the *ab initio* data described below. The spectator potential V_s is a sum of two terms,

$$V_s = V_u(u)_{x_0,y_0,z_0,\tau_0,\vartheta_0} + V_\theta[\theta(x)]_{y_0,z_0,\tau_0}. \quad (8)$$

Here V_u is a Morse potential given by,

$$V_u(u) = D_e[1 - e^{-b(u-u_0)}]^2, \quad (9)$$

with fit parameters $\{D_e,u_0,b\}$. The other part of the spectator potential V_θ is given by,

$$V_\theta[\theta(x)] = [A(\cos\theta - \cos\theta_1)^4 + B(\cos\theta - \cos\theta_1)^3]e^{-\alpha(x-x_1)}, \quad (10)$$

where

$$\theta_1 = C + De^{-\alpha'(x-x_1)} \quad (11)$$

with fit parameters $\{A,B,C,D,\alpha,\alpha',x_1\}$. The functional form of Eq. (10) is slightly different from the study of Wu *et al.*[25] to better match the *ab initio* $O+H_2O$ surfaces.

Since functional forms for the H_2O reagents[27] and OH products[28] have already been developed which match experimental data very well, we incorporate these known potentials in the present global fit. We do this in a similar fashion to Wu *et al.*[25] by employing switching functions that turn on and off the reagent, product, and V_{a+s} potentials in appropriate regions. We choose the following forms for these switching functions:

$$S_r = \tfrac{1}{2}\{1 + \tanh[r_0(y - r_1)]\}, \quad (12a)$$

$$S_q = \tfrac{1}{2}\{1 + \tanh[(y - x)]\}, \quad (12b)$$

$$S_p = \tfrac{1}{2}\{1 + \tanh[p_0(x - p_1)]\}, \quad (12c)$$

with fit parameters $\{r_0,r_1,p_0,p_1\}$. Defining V_r to be the isolated H_2O potential, and V_p as the potential of two isolated OH products, the global potential can then be expressed as

$$V_{\text{unsym}} \propto S_rS_qV_r + [1 - S_rS_q - S_p(1 - S_q)]V_{a+s} + S_p(1 - S_q)V_p. \quad (13)$$

An undesired side effect of separating active and internal coordinate potentials is that the potential V_{unsym} treats the hydrogen atoms on the water reagent in an unsymmetrical fashion. This means that the potential V_{unsym} is different depending on whether the incoming oxygen attacks H_b rather than H_a, which is unphysical. To compensate, we follow Wu *et al.*[25] and introduce the switching function S_s, which makes attack on either hydrogen equivalent.

$$S_s = \tfrac{1}{2}\{1 - \tanh[s_0(R_{O_bH_a} - R_{O_bH_b})]\}. \quad (14)$$

where $\{s_0\}$ is a fit parameter. The full global symmetrized potential is then the weighted sum of two unsymmetrized parts,

$$V_{\text{sym}} = S_sV_{\text{unsym}}(H_a\text{–}O_a\text{–}H_b + O_b) + (1 - S_s)V_{\text{unsym}}(H_b\text{–}O_a\text{–}H_a + O_b), \quad (15)$$

where $V_{\text{unsym}}(H_a\text{–}O_a\text{–}H_b+O_b)$ is the potential of the atoms in their original configuration, and $V_{\text{unsym}}(H_b\text{–}O_a\text{–}H_a+O_b)$ is the potential with the H atoms switched. This is essentially an averaging of two geometric configurations.

Table I gives the values of all the parameters for the potential for all three electronic states and how they were derived. Many of the values were obtained from *ab initio* calculations described in the following section.

3. Electronic structure calculations

Most of our *ab initio* calculations were based on a 10 electron 8 orbital (10*e*8*o*) CASSCF+MP2 treatment with a (4*s*3*p*2*d*1*f*) O-atom basis and (3*s*2*p*) H-atom basis for a total of 90 basis functions. The (10*e*8*o*) CASSCF includes all excitations of ten electrons within the space of an initial configuration of two bonding, two lone pair, two singly occupied, and two un occupied antibonding orbitals. (The 1*s* and 2*s* oxygen orbitals are not included in the CASSCF space.) This totals 1512 configuration state functions. We state average the three lowest electronic states and perform all these calculations with no symmetry. This choice of CASSCF space ensures that the three electronic states treated will be degenerate on the reagent and product sides of the reaction as they should be, and that the CASSCF space includes bonding and antibonding orbitals so that OH bonds can break and form in an even handed way along the reaction path. A summary of the electronic energies and energy differences of the reagents, products, and at the lowest transition state geometry of state 1 (as determined from the study of Ref. 17) are given in Table II. All calculations were done with the GAMESS electronic structure package.[29]

The experimental T_e leading to OH+OH is 14.7 kcal mol^{-1} which is 0.9 kcal mol^{-1} below the present calculated *ab initio* results. Because we use switching func-

TABLE I. Surface fit parameters. All values are in a.u.

Fit parameters	Values (a.u.)	How determined
State 1 transition state geometry $\{x_0, y_0, z_0, u_0, \theta_0, \tau_0\}$	(2.3501, 2.0558, 141.06°, 1.8287, 104.55°, 0.0)	Reference 17
$W(\tau)$, $\{a_0, \ldots, a_6\}$		Fit of *ab initio* data
State 1	(0.672, 0.649, −0.311, −0.347, 0.373, 0.198, −0.234)	
State 2	(1.47, −0.296, −0.387,0.511, −0.0724, 0.263, −0.496)	
State 3	(3.63,0.480, −5.74, −0.614, 5.15, 0.627, −2.55)	
$V_u\{D_e, b, u_0\}$		Fit of *ab initio* data
State 1	(0.1628, 1.2200, 1.8500)	
State 2	(0.1757, 1.2644, 1.8287)	
State 3	(0.1574, 1.3000, 1.8286)	
$V_\theta\{A, B, C, D, \alpha, \alpha', x_1\}$		Fit of *ab initio* data
State 1	(0.7400, 0.065, 99.0, 110, 1.9, 1.6, 2.11)	
State 2	(0.221, 0.0164, 98.7, 3.3, 1.0525, 0.8, 2.232)	
State 3	(0.137, −0.0416, 103.5, 16., 2.307, 0.1, 2.35)	
Switching functions $\{r_0, r_1, p_0, p_1, s_0\}$	(4.0, 6.0, 3.0, 4.0, 3.0)	Reference 25
OH product $\{D_e, b, u_0\}$	(0.1698, 1.21, 1.85)	Reference 28
H_2O reagent	Many	Reference 27
V_{spline} coefficients	Many	Fit of *ab initio* data

tions to smoothly connect to the reagent and product parts of the potential, we have defined the T_e for the present fitted potential to be the experimentally measured T_e of 14.7 kcal mol^{-1}. Computing transition state geometries at the CASSCF-MP2 level is problematic, especially with state averaging. So we have adopted the transition state geometry for state 1 reported in Ref. 17 which uses a basis set extrapolation technique within a QCISD(T) treatment. Reference 17 obtained a T_e for the transition state of state 1 of +1.61 kcal mol^{-1} above the OH+OH limit, while the present surface would be nearly equal in energy to the OH+OH limit for the lowest triplet. Deyerl *et al.*[19] obtain a lowest triplet transition state very similar in geometry to Karkach *et al.* within a QCISD(T)/6-311++G($3df,2p$) treatment which is +0.10 kcal mol^{-1} above the OH+OH limit (electronic energy −151.315 271). As discussed further below, the second and third lowest triplets have potential surfaces quite similar to the lowest triplet, except that the barrier heights are larger by ~10 and ~15 kcal mol^{-1}, respectively. The second and third states should therefore play a role at hyperthermal energies.

To obtain the spline fit parameters, GAMESS CASSCF +MP2 calculations were done on a $34\times34\times14$ grid of x,y, and z points for a total of 16 184 points. For these calculations ($\theta=104.5°, u=1.8085$ a.u., $\tau=0°$). The values of u and θ are slightly different from the transition state geometry adopted here but these differences will have minimal impact on the fit. The x and y coordinate grid spanned the range 1.3228 a.u.–7.559 a.u. with spacings of 0.1890 a.u. in each direction. The z-coordinate values extend from 50° to 310° with a spacing of 20°. We fit the computed energies to a 3D cubic spline (with tension) after Ref. 26. For geometries lying outside the x- and y-value grid points, we map the results to the nearest extreme grid value. For z values outside the calculated range, we perform a linear interpolation between the nearest extreme grid values. Also, for $z\in[50°,70°]$ we found it necessary to use a multidimensional linear (rather spline fit) to avoid unphysical oscillations in the interpolated potential. We note the cubic spline interpolation is simultaneously performed for all three active coordinates, so the z coordinate is treated on equal footing with the x and y coordinates. We also note that for subsequent dynamics calculations, splines are especially efficient for evaluations of the potential as all interpolations are performed locally while the value of the function and its first derivative remain continuous from one grid point to the next.

TABLE II. Computed CASSCF-MP2 Energies. T_e is defined to be the calculated energy difference with respect to $O+H_2O(R_e)$, Energy−Energy $[O+H_2O(R_e)]$.

Geometry	Energy (a.u.)	T_e (kcal mol^{-1})
$O+H_2O(R_e)$	−151.289431	0.0
$OH(R_e)+OH(R_e)$	−151.264587	15.59
Transition state for state 1 (Following Ref. 17; Table I)		
State 1	−151.266 063	14.66
State 2	−151.250 827	24.22
State 3	−151.227 117	39.10

To obtain the $W(\tau)$ fit parameters for each state, we performed CASSCF+MP2 calculations as described above fixing all internal coordinates except τ to the transition state geometry. We then varied τ in steps varying from 5° to 20° from 0° to 180°. Similarly, to obtain the V_u fit we performed CASSCF+MP2 calculations fixing all internal coordinates except u to the transition state geometry and varied u over 61 points in the range 1.22–9.44 a.u. For the V_θ fit we performed a series of CASSCF+MP2 calculations fixing all internal coordinates except θ and x at their transition state geometries. We varied θ and x on a two-dimensional grid, varying θ every 5° from 0° to 360° and varying x from 1.16 to 8.019 a.u. over 24 unevenly spaced steps. Since V_{spline} already contains a dependence on x, we fit the residual dependence, $V_{ab\ initio}-V_{\text{spline}}$ in order to isolate the contribution of varying the spectator coordinate θ.

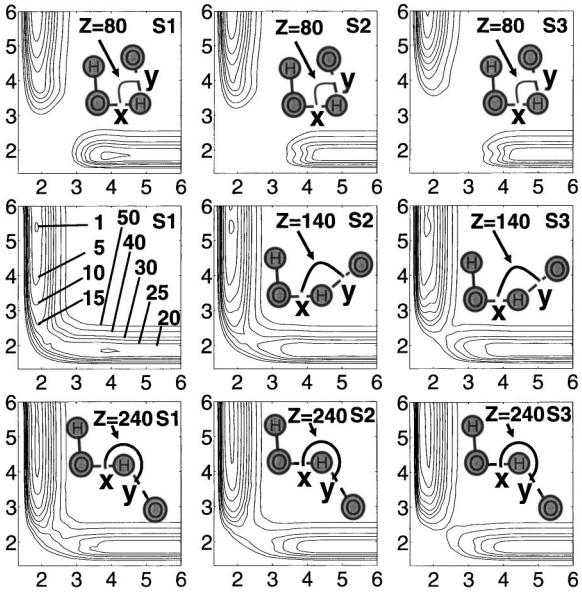

FIG. 3. Fitted potential energy surfaces of the three lowest triplet states of the $O(^3P)+H_2O(X\,^1A_1)$ system. In each frame, the abscissa is the x coordinate and the ordinate is the y coordinate. Each column shows a different electronic state, $S1$ corresponds to state 1, $S2$ to state 2, and $S3$ to state 3. Each row shows a different fixed z coordinate (80°, 140°, and 240°). The spectator coordinates $\{u,\theta,\tau\}$ are fixed at the transition state values of state 1, as determined in Ref. 17. Contour levels in all frames are at $\{1,5,10,15,20,25,30,40,50\}$ kcal mol^{-1} with respect to $O+H_2O(R_e)$, as explicitly labeled for $S1$ $z=140°$. Distances are in a.u.

4. Properties of potential surfaces

The potential surface fits for the three lowest triplet states of the $O+H_2O$ system are shown in Fig. 3 for planar geometries. In Fig. 3, the spectator coordinates $\{u,\theta,\tau\}$ are fixed at the transition state values of state 1 as determined in Ref. 17 and listed in Table I. We have not determined transition state geometries because this is problematic with state averaging as was done here. We have simply used the state 1 transition state from Ref. 17 as a convenient reference geometry for separating the active and spectator fits. The spectator coordinates are fixed in order to isolate the V_a portion of the potential. The z coordinate is fixed at 80°, 140°, and 240°. The active coordinate $\{x\}$ varies along the abscissa. The active coordinate $\{y\}$ varies along the ordinate. Large values of y correspond to the separated $O+H_2O$ reagents and large values of x correspond to separated OH+OH products. The transition state barrier for this fitted potential occurs near $z=140°$ for all three surfaces and its energies are ~15, ~24, and ~39 kcal mol^{-1}, respectively, with respect to $O+H_2O(R_e)$. The transition state saddle point for the lowest state occurs near $x\approx 2.4$ and $y\approx 2.1$ a.u., so that the OH bond that is breaking along x is longer than the OH bond that is forming along y. Figure 4 shows the fitted potential V_a for nonplanar geometries for all three fitted surfaces. In Fig. 4, all coordinates are fixed at their transition state values as shown in Table I, and the torsion angle τ is varied from 0° to 180° to isolate the effect of out-of-plane motion. For the lowest electronic state there is a preference for 0° (*cis*) geometries over 180° (*gauche*) by ~7 kcal mol^{-1}. There appears to be an avoided crossing near $\tau=130°$ between the two lowest electronic states. For the third electronic state

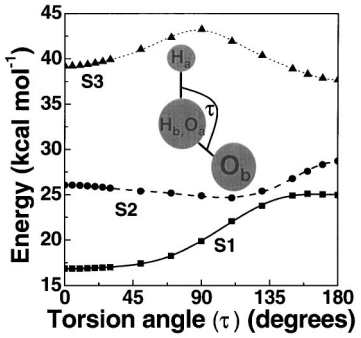

FIG. 4. The τ (out of plane) dependence of the active potential, V_a for the three lowest triplet states of the $O(^3P)+H_2O(X\,^1A_1)$ system. Here it is defined with respect to the energy of V_a for state 1 at the transition state geometry given in Table I. $S1$ corresponds to state 1 (■), $S2$ to state 2 (●), and $S3$ to state 3 (▲).

there is an energy maximum near $\tau=90°$ and the 0° and 180° geometries have about the same energy. The barriers for out-of-plane motion are generally small.

Figure 5 shows the V_θ component of the spectator potential, which is sensitive to the reagent H_2O internal bond angle, for all three fitted surfaces. For these plots, all internal coordinates except θ are fixed at their transition state values as given in Table I. For all three surfaces there is a barrier at linear H_2O geometries, which is ~30 kcal mol^{-1} for the lowest electronic state. There are local minima at $\theta\approx 104.5°$ and $\theta\approx 255.5°$ which correspond to *cis* and *trans* geometries of the combined $O+H_2O$ system where the reagent is close to its isolated equilibrium bond angle. V_θ is constructed to be zero here as the V_a part of the potential already treats these geometries. Small and large values of θ correspond to "small angle" geometries of the reagent H_2O, and so are dominated by the nuclear-nuclear repulsions of the H_2O hydrogens. Figure 5 is for fixed a value of x. As x increases and products are formed, V_θ retains the same shape but decreases in magnitude for all three states as expected.

Figure 6 shows the full potential for all three fitted states, $V_{\rm sym}$ for planar geometries. In Fig. 6, the coordinates $\{x,u,\theta,\tau\}$ have been fixed at their transition state values as shown in Table I, and $\{y,z\}$ have been allowed to vary. This view shows the potential for a fixed H_2O reagent at varying angles of approach of the O atom. The chief feature of these surfaces is a well near angles of approach corresponding to

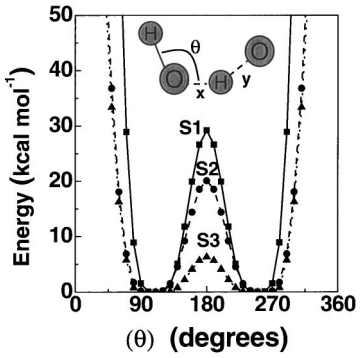

FIG. 5. The V_θ portion of the spectator potential V_s as a function of θ for the three lowest triplet states of the $O(^3P)+H_2O(X\,^1A_1)$ system. $S1$ corresponds to state 1 (■), $S2$ to state 2 (●), and $S3$ to state 3 (▲).

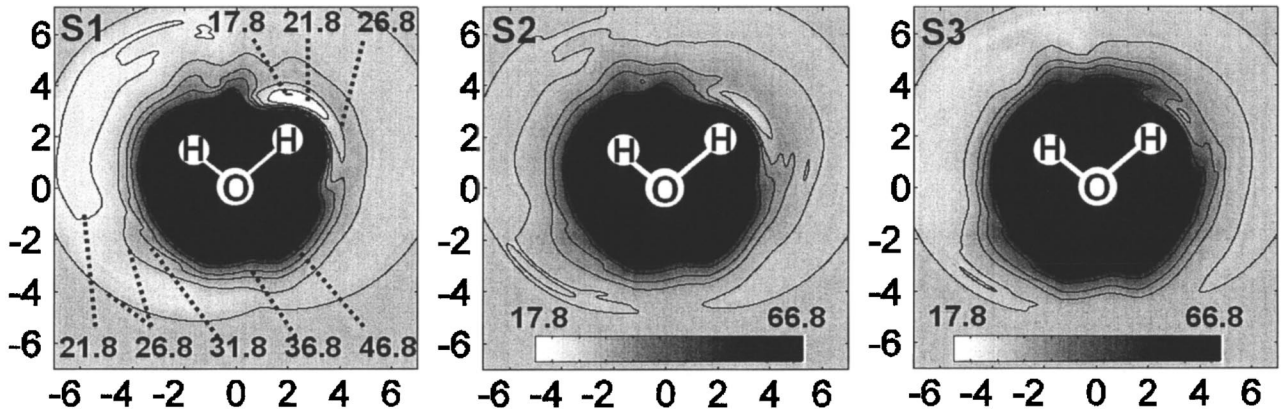

FIG. 6. Full potential V_{sym} for planar geometries of the $O(^3P)+H_2O(X\,^1A_1)$ system where the reagent H_2O bond lengths and angles are fixed at the transition state geometry for state 1, as shown in Table I, for the three lowest triplet adiabatic states *S*1, *S*2, and *S*3. The position of the approaching reagent O atom is varied along the abscissa and ordinate coordinates. The atom positions of the H_2O reagent are explicitly shown and are fixed in all frames. Distances are in a.u. Contour values are at $\{1,5,10,15,20,30,40,50\}+16.8$ kcal mol^{-1} with respect to $O+H_2O(R_e)$, as explicitly labeled for *S*1.

cis geometries of the $O+H_2O$ system, in regions centered near $z\approx 140°$ for the lowest electronic state. For the higher electronic states the well is not so deep and $z\approx 180°$. These z angles are the preferred angles of approach of the O atoms for chemical reaction. As the reagent OH bond lengthens (x increases) and the product OH bond forms (y decreases) the shallow wells in Fig. 6 deepen. In a simple molecular orbital picture for in-plane geometries near the transition state of state 1, the two singly occupied p orbitals can form bonding interactions with the H atoms of the reagent H_2O for the lowest electronic state. In the second lowest electronic state, one of the singly occupied p orbitals can interact with the closest H atom of water, and in the third electronic state, the nonbonding p orbital of the O atom has a mostly repulsive interaction with the H atom of H_2O. Generally, other angles of approach are repulsive, except at large distances where there are shallow long-range-type interactions of the approaching oxygen and H_2O hydrogens.[30] Some of this long-range attraction corresponds to geometries affected by our separation of active and spectator coordinates and the way the present potential is symmetrized, and so we do not expect these regions to be as accurate as the transition state geometry regions which are fit by splines alone.

B. QCT calculations

We use the VENUS classical trajectory code[31] with an added interface modification in order to use our fitted potential surfaces and derivatives to generate rate constants and cross sections. For all calculations we use a fixed time step of $\delta t=1E-16$ seconds and a maximum impact parameter b_{max} ranging from 5.7 a.u. to 7.56 a.u. To generate rate constants at fixed temperatures, we perform 1E5 to 5E5 trajectories per electronic state per temperature. To generate cross sections at fixed translational energies, we fix the reagent water in its ground rovibrational state and perform 1E5 to 5E5 trajectories per each electronic state per energy. To obtain total rate constants or cross sections we add the trajectory contributions from each electronic state together and multiply by 1/3, the electronic degeneracy factor. This approach assumes no electronic, spin-orbit, or Coriolis coupling between the surfaces, an assumption we make to simplify the dynamics calculations. In fact, regions of the surfaces are energetically close enough that coupling between the surfaces could affect the detailed product distributions. We will explore such coupling in future work. For final state-resolved quantities the $OH(\nu,j)$ states are binned in the usual way as outlined in Ref. 31. Final H_2O products are binned according to the amount of internal energy in rotation and vibration. We note that our results do not adjust for zero-point energy of the reagents, which will sometimes tend to make such classical dynamical results more "reactive" than the potential actually allows.

III. RESULTS AND DISCUSSION

A. Rate constants at fixed temperatures for $O(^3P)+H_2O(X\,^1A_1)\rightarrow OH(X\,^2\Pi)+OH(X\,^2\Pi)$

Figure 7 shows the computed QCT rate constant k_{rxn}, for the reaction $O(^3P)+H_2O(X\,^1A_1)\rightarrow OH(X\,^2\Pi)+OH(X\,^2\Pi)$, as a function of temperature together with data from two

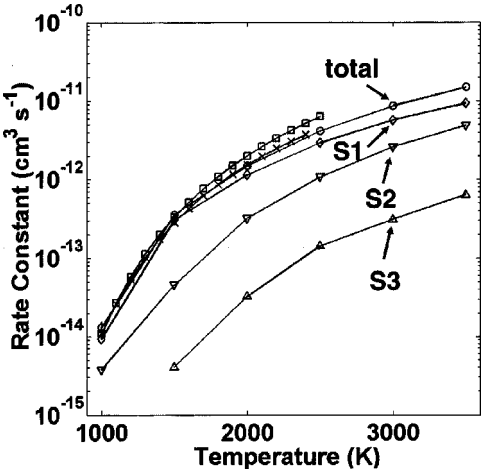

FIG. 7. Rate constant as a function of temperature for the reaction $O(^3P)+H_2O(X\,^1A_1)\rightarrow OH(X\,^2\Pi)+OH(X\,^2\Pi)$. □, experimental results of Ref. 22; ×, experimental results of Ref. 23; ◯, total calculated results including contributions from all three states; ◇, contribution from state 1 (*S*1); ▽, contribution from state 2 (*S*2); △, contribution from state 3 (*S*3).

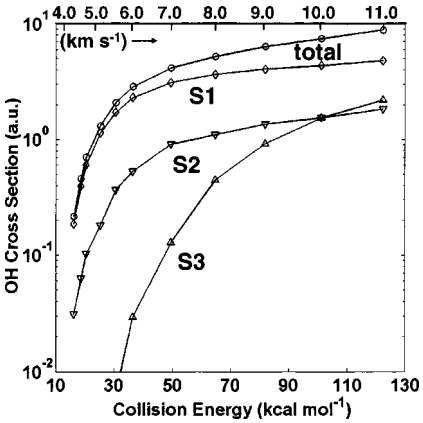

FIG. 8. Total calculated OH cross section as a function of collision energy for the reaction $O(^3P)+H_2O(X\,^1A_1)\rightarrow OH(X\,^2\Pi)+OH(X\,^2\Pi)$ according to Eq. (16): ◯, total calculated results including contributions from all three states; ◇, contribution from state 1 (*S*1); ▽, contribution from state 2 (*S*2); △, contribution from state 3 (*S*3). Relative collision velocity is shown on the top scale.

measurements.[22,23] Calculations were performed from 1000 K to 3500 K at intervals of 500 K. There is good agreement between the present results and measurements[22,23] (especially Ref. 23), with the present results mostly within experimental uncertainties (about a factor 2). Usually, neglect of a zero-point energy correction as in the present QCT calculations would tend to overestimate the rate constant but there may be a compensating error in the neglect of a tunneling correction. We do not report results below 1000 K because of the difficulty of obtaining acceptable QCT statistics. The separate electronic state contributions to the QCT computed rate constant are also shown. The dominant contribution is from the lowest energy electronic state, state 1, as expected. The second lowest electronic state also makes an appreciable contribution at all temperatures studied and at the highest temperatures has a contribution within a factor of 2 of state 1.

B. Cross sections at fixed collision energies for $O(^3P)+H_2O(X\,^1A_1)\rightarrow OH(X\,^2\Pi)+OH(X\,^2\Pi)$

1. Total and vibrationally resolved cross sections

Figure 8 shows the total calculated QCT "OH cross section," σ_{OH} for the reaction $O(^3P)+H_2O(X\,^1A_1)\rightarrow OH(X\,^2\Pi)+OH(X\,^2\Pi)$, as a function of collision energy along with component contributions from the three lowest triplet electronic states. Calculations were performed at the following collisions energies: 16.2, 18.7, 20.5, 25.3, 30.6, 36.4, 49.6, 64.8, 82.0, 101.2, and 122.5 kcal mol^{-1} which correspond to relative collision velocities of 4.0, 4.3, 4.5, 5.0, 5.5, 6.0, 7.0, 8.0, 9.0, 10.0, and 11 km s^{-1}. We define the OH cross section σ_{OH} in the following way:

$$\sigma_{OH}=2\sigma_{rxn}=\pi b_{max}^2\frac{2N_r}{N_{tot}}, \tag{16}$$

where σ_{rxn} is the reaction cross section, N_r is the number of reactive QCT trajectories, and N_{tot} is the total number of trajectories. The cross section σ_{OH} is more convenient for comparisons to most of the available measurements which often report absolute cross sections by detecting and adding together signals from both OH products formed in the reaction. The OH cross section is relatively small near threshold and increases with energy. By 30 kcal mol^{-1} collision energy, the cross section is relatively constant, although it continues to increase with collision energy. This implies that future measurements need to start below 5 km s^{-1} to capture the rapid increase of the excitation function near threshold. As

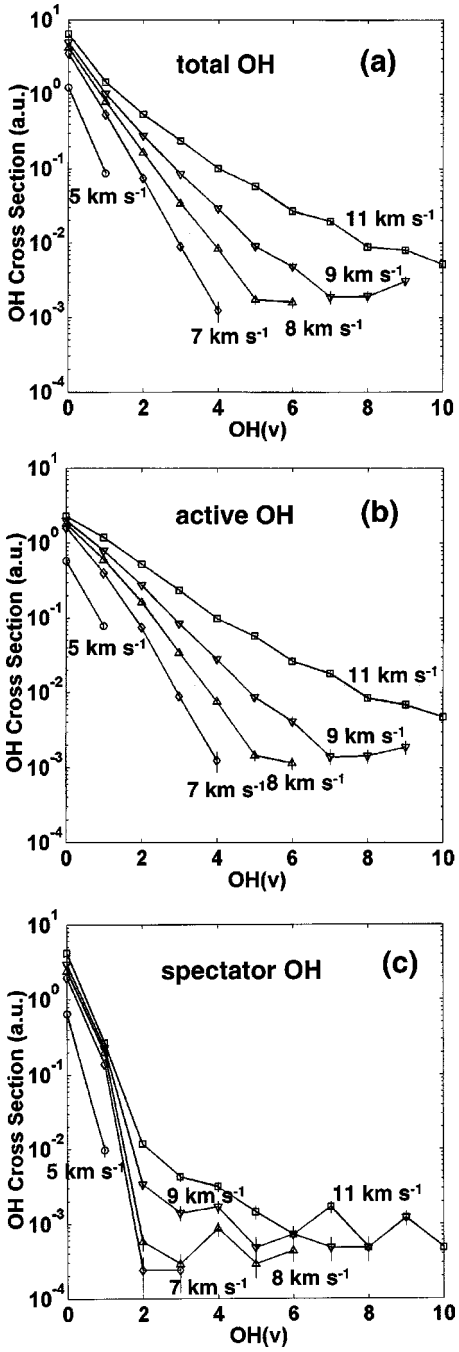

FIG. 9. (a) Calculated vibrationally resolved cross sections as a function of collision velocity for the reaction $O+H_2O\rightarrow OH(v)+OH(v)$ according to Eq. (16). For a given v, contributions from both $OH(v)$ products are summed. (a) ◯, results at 5 km s^{-1} collision velocity; ◇, results at 7 km s^{-1} collision velocity; △, results at 8 km s^{-1} collision velocity; ▽, results at 9 km s^{-1} collision velocity; □, results at 11 km s^{-1} collision velocity. (b) Same as (a) except results only include $OH(v)$ products formed from the incoming O-atom reagent (active OH). (c) Same as (a) except results only include $OH(v)$ products formed from reagent H_2O O atom (spectator OH).

the energy increases past the energy barriers of state 2 and state 3, they begin to contribute significantly to the cross section. At the highest collision energies studied, the contribution from state 3 becomes comparable to that of state 2, where they are about 2.5 times smaller than state 1.

Figure 9(a) shows the QCT vibrationally resolved OH cross sections $\sigma_{OH}(v)$ for the reaction $O(^3P)+H_2O(X\,^1A_1)\rightarrow OH(X\,^2\Pi)+OH(X\,^2\Pi)$ at 25.3, 49.6, 64.8, 82.0, and 122.5 kcal mol^{-1} collision energy or 5.0, 7.0, 8.0, 9.0, and 11.0 km s^{-1} collision velocity, respectively, where we have summed the contributions from both OH products in a particular vibrational state [Eq. (16)]. At 5,7, and 8 km s^{-1} collision velocity, the distributions are well fit by thermal populations with temperatures of 1900 K, 2700 K, and 3100 K, respectively. At 9 and 11 km s^{-1} collision velocity we can fit the lower OH(v) states both with thermal temperatures of ~3500 K. The highest OH(v) populations for these higher velocities begin to show a different type of distribution. However these cross sections are very low, and proper fitting of this population requires better statistics. Figures 9(b) and 9(c) show the component "active" and "spectator" vibrationally resolved OH cross sections. The active OH products are from the incoming reagent atomic oxygen, and the spectator OH products are made from the oxygen in the reagent H_2O, so that the total OH cross section [Fig. 9(a)] for a given vibrational level is the sum of active and spectator OH cross sections for that level. Although measurements of the active and spectator OH cross sections would probably only be available through detailed molecular beam isotopic studies, the computed active and spectator OH cross sections offer insight into the dynamics of the collision process. For example, it is clear that the active and spectator vibrationally resolved OH cross sections are quite distinct. The spectator cross sections are significantly colder than the active OH populations. The spectator OH's mainly populate OH($v=0,1$) levels, with the $v=1$ relative populations significantly less than that of the active OH($v=1$) populations. The spectator OH($v>1$) populations are almost negligible. This means that the total OH($v>0$) populations are due almost exclusively to the active OH, and the total OH($v=0$) populations are mainly due to the spectator OH. The OH bond being formed in the reaction takes up most of the vibrational energy in the products. Joint active/spectator distributions would reveal more detailed information, but would require substantially better statistics.

The vibrationally resolved results of Fig. 9(a) can be compared with data. Fixed energy spaced-based and laboratory measurements for $O(^3P)+H_2O(X\,^1A_1)\rightarrow OH(X\,^2\Pi)+OH(X\,^2\Pi)$ focus on the detection of infrared radiation from vibrationally excited total OH [active + spectator, Fig. 9(a)] products summed over the populated vibrational states. Since the available spaced-based and laboratory measurements do not measure vibrationally resolved cross sections directly, it is necessary to briefly review the nature of these experiments to make appropriate comparisons with the present results.

As outlined in Ref. 7, space-based measurements (such as those of Refs. 5, 6, and 9) are characterized by a steady-state outgassing or exhausting source of H_2O with a known or assumed rate, N_{H_2O} (number of H_2O per second), interacting with atomic oxygen in the atmosphere. The signal is usually observed through a somewhat opaque atmosphere integrated over a wavelength band and characterized by a transmittance $T_{\Delta\lambda}$. The observed steady-state intensity, $I_{\Delta\lambda}^{space}$ (photons/second), can be written as

$$I_{\Delta\lambda}^{space} \propto \left[\frac{\sigma^*}{\sigma_{tot}}\right] N_{H_2O} T_{\Delta\lambda}, \tag{17}$$

where σ_{tot} is the total (reactive and nonreactive) collision cross section for $O+H_2O$ and σ^* is the photon excitation cross section which includes all contributions due to photon cascades from multiquantum excited states. For detection in the 2–5 μ spectral region where most of the relevant optical measurements take place for this system, the intensity will be sensitive to single vibrational quantum changes, so we write σ^* as

$$\sigma^* = \sum_{species} \sum_{v=1} v\sigma_v^{species}, \tag{18}$$

where v is the vibrational quantum number, $\sigma_v^{species}$ is the cross section to a particular vibrational state of either collisionally excited H_2O or reaction product OH radiating in the detection band. It is important to emphasize that observations usually include contributions from both species, and so the first sum extends over OH and H_2O. The second sum extends over all possible excited vibrational levels of a given species. Space-based measurements usually assume or otherwise employ models to estimate values for N_{H_2O}, $T_{\Delta\lambda}$ and σ_{tot}, and from the observed intensity $I_{\Delta\lambda}^{space}$ report a photon excitation cross section σ^*. Therefore, uncertainties in the estimated values of N_{H_2O}, $T_{\Delta\lambda}$ and σ_{tot} are reflected in the reported σ^*.

On the other hand, ground-based laboratory measurements involving optical detection typically use pulsed beam sources. Signals, $I_{\Delta\lambda}^{lab}$, from such measurements are related to the photon excitation cross section in the following way:

$$I_{\Delta\lambda}^{lab} \propto \sum_{species} \sum_{v=1} A_v^{species} \sigma_v^{species}, \tag{19}$$

where $A_v^{species}$ are Einstein coefficients (photons/second) for single photon radiative decay. Because contributions from separate species and from individual vibrational levels usually cannot be distinguished, lab measurements typically report a single value for the right-hand side double sum of Eq. (19) at fixed $O+H_2O$ collision velocities. We note that these laboratory measurements are often difficult to carry out and calibrate absolutely with high precision due to uncertainties in reactant concentrations and the inability of optical systems to capture all collision produced photons within a limited field of view.

Table III gives two space-based results for the photon excitation cross section [Eq. (18)], two laboratory results for the product cross sections times Einstein A [Eq. (19)], and the corresponding quantities derived from the present calculated vibrationally resolved total OH cross section [Fig. 9(a)]. These quantities follow the analysis of Ref. 7 and assume $A_v^{OH}=v17\ s^{-1}$. It is estimated that the experimental results are uncertain by a factor of between 2 and 3. At 4.3 km s^{-1}, the laboratory results of Ref. 1 are about 12 times larger than the presently computed contribution from excited

TABLE III. Excitation cross sections derived from space-based, laboratory, and presently calculated results (theory) for $O(^3P)+H_2O(X\,^1A_1)$ collisions to produce radiation from 2–5 μ.

Relative collision velocity (km s^{-1})	$\Sigma_{v=1} v\sigma_v^{OH}$ Theory (a.u.)	$\Sigma_{species}\Sigma_{v=1} v\sigma_v^{species}$ Space Expt. (a.u.)	$\Sigma_{v=1} A_v^{OH}\sigma_v^{OH}$ Theory (a.u./s).	$\Sigma_{species}\Sigma_{v=1} A_v^{species}\sigma_v^{species}$ Lab Expt. (a.u./s)
4.3			0.09	1.07[a]
~8.0	1.28	0.54[b]	21.75	18.20[c]
11	4.41	3.57[d]		

[a]Reference 1.
[b]Reference 6.
[c]Reference 4.
[d]Reference 9.

OH. This collision energy is too low to excite OH populations. Therefore, the experimental signal is nearly all H_2O, collisionally excited in the v_1 and v_3 stretching modes. At 8 km s^{-1}, well above the reaction energy barrier to make OH, the measured space-based[6] results are about a factor of 2 smaller than laboratory results.[4] The laboratory results are about equal to the presently computed OH contribution to the overall signal. At 11 km s^{-1} there is good agreement between the space-based combined signal and presently computed contribution from OH. The present results therefore imply that at and above 8 km s^{-1} collision velocity, the OH contribution is at least comparable and perhaps larger than the H_2O contribution to the observed infrared signals. We note that the H_2O collisional excitation cross sections have been computed in previous studies. Although these studies used the same nonreactive potential surface, the quantum scattering results of Ref. 14 differ by orders of magnitude from the classical scattering results of Ref. 13 even at high velocities, so it is difficult to assess the possible relative contributions from collisionally excited water. We note, however, that at 8 km s^{-1} collision velocity there is fairly good agreement between the quantum results for collisional excitation of H_2O and the measurements of Ref. 4. With the presently computed contribution from OH, the theoretically derived combined H_2O/OH would still be within the experimental error bounds.

We note that the vibrational temperature of 3100 K obtained from the present calculations at 8.0 km s^{-1} is quite different from what has been conjectured by Bernstein *et al.*[7] in their fit of observed spectra of Ref. 4 obtained in hyperthermal O-atom beam experiments at similar collision energies. Bernstein *et al.*[7] derive a vibrational temperature of 7000 K, which was mostly driven by the observed large OH overtone signals. The present results cannot reproduce the apparently large overtone populations observed in Ref. 4. We note, however, that because the O-atom beam experiments use a finite field of view, OH products with lower translational energies (higher vibrational energies) may be weighted more than higher translational energy products (lower vibrational energies) that quickly escape from the field of view. These effects, not accounted for in the present analysis, may explain the hotter observed vibrational populations.

2. Rotationally resolved cross sections

Figure 10 shows the rotationally resolved total OH cross section at 5.0, 7.0, 8.0, 9.0, and 11.0 km s^{-1} relative collision velocity for $O(^3P)+H_2O(X\,^1A_1)\rightarrow OH(X\,^2\Pi)+OH(X\,^2\Pi)$, where the $OH(v)$ populations have been summed over. These

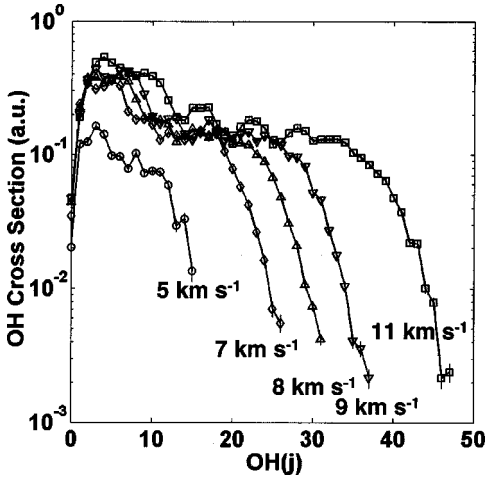

FIG. 10. Calculated rotationally resolved cross sections as a function of collision velocity for the reaction $O+H_2O\rightarrow OH(j)+OH(j)$ according to Eq. (16). For a given OH rotational level j, contributions from both active and spectator OH products are summed over all $OH(v)$ vibrational levels. ◯, results at 5 km s^{-1} collision velocity; ◇, results at 7 km s^{-1} collision velocity; △, results at 8 km s^{-1} collision velocity; ▽, results at 9 km s^{-1} collision velocity; □, results at 11 km s^{-1} collision velocity.

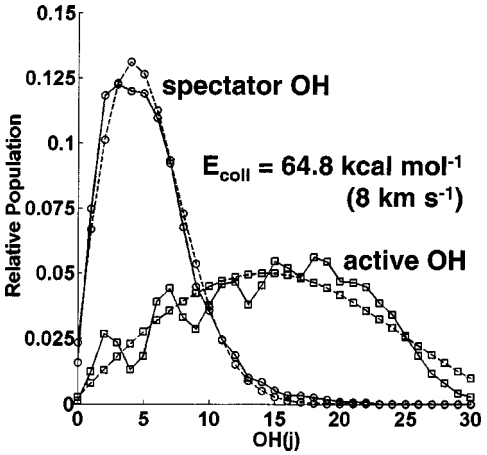

FIG. 11. Calculated relative populations at 8 km s^{-1} relative collision velocity for the reaction $O+H_2O\rightarrow OH_{active}(j)+OH_{spectator}(j)$. —□—, presents results for $OH_{active}(j)$; - -□- -surprisal theory, Eq. (20), with $\theta_r=0.0$; —◯—, presents results for $OH_{spectator}(j)$; - -◯- -surprisal theory, Eq. (20), with $\theta_r=-0.41$.

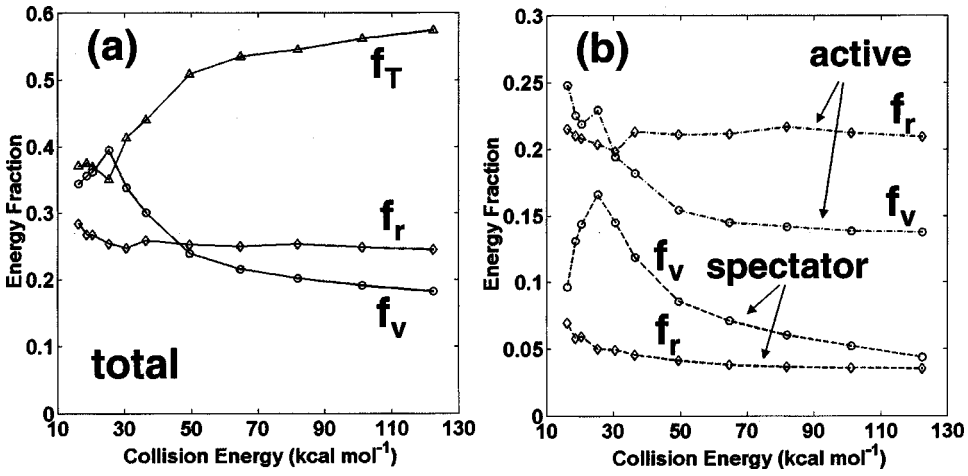

FIG. 12. Calculated product energy fraction as a function of collision energy for the reaction $O(^3P)+H_2O(X\,^1A_1)\rightarrow OH(X\,^2\Pi)+OH(X\,^2\Pi)$. (a) Total summed over OH active and spectator contributions, —△—, translational energy fraction f_T; —◇—, rotational energy fraction f_r; —◯—, vibrational energy fraction f_v. (b) Active OH and spectator OH contributions to the internal energy fraction.

cross sections show a bimodel distribution, a narrow low OH($j<10$) peak and a wide almost flat OH(j) extending to very high OH(j) which eventually falls off as the energetic limit is reached. As shown in Fig. 11 for 8 km s^{-1} collision velocity, the two underlying rotational distributions come from the active and spectator OH's. The active OH is much more rotationally excited than the spectator OH, so that the active OH receives the vast majority of the internal energy imparted to products in the collision. The superimposed oscillatory structure for low active OH(j) populations appears to be real and not caused by statistical uncertainty.

We have fit the separate active and spectator OH(j) rotational populations to a distribution derived from surprisal theory,[32]

$$P(vj) \propto \exp(\theta_r E_{vj})(2j+1)\sum_{ml}(2l+1)(E-E_{vj}-E_{ml})^{1/2}, \tag{20}$$

where (vj) are the vibrational and rotational quantum numbers, respectively, for OH product being fit, (ml) are the vibrational and rotational quantum numbers, respectively, for the other OH product, E is the total energy available to be distributed to products in the reaction, θ_r is a surprisal parameter, the sum of (ml) extends over all the available energy states, and we have set $v=0$. The results are shown in Fig. 11 for separate fits to the active and spectator OH's, where $\theta_r=0.0$ (statistical) for the active OH and $\theta_r=-0.41$ for the spectator OH. We note that the peak OH(j) products correspond to rotational temperatures of 11 400 K and 1100 K for the active and spectator OH's, respectively. The analysis of Ref. 7 of the data in Ref. 4 derives a rotational temperature for total OH of 1500 K. This temperature should be dominated by the active vibrationally excited OH for which we calculate a much higher rotational temperature. A more accurate temperature comparison with measurements would weight the contributions of the calculated OH(v,j) states by their Einstein A coefficients and account for finite field of view effects. These combined effects may improve agreement with experiment, but the calculated results would still likely be hotter than the observations.

3. Product energy disposal

Figure 12(a) shows the total OH and Fig. 12(b) shows the active and spectator OH energy disposal shown as energy fractions of translation, vibration, and rotation, as a function of the collision energy. We define the total energy, $E=E_{\mathrm{coll}}+E\mathrm{z.p.}(H_2O)-14.7$ kcal mol^{-1}, and the energy fractions as $f_v=\langle E_v\rangle/E$, $f_r=\langle E_r\rangle/E$, and $f_T=1-\langle f_v\rangle-\langle f_r\rangle$. We note that the average energies, $\langle E_v\rangle$, and $\langle E_r\rangle$, were obtained before histogram binning and are summed over all trajectories with the appropriate weighting of electronic state contributions. For the total OH energy disposal at energies below ~35 kcal mol^{-1} the vibrational and translation fractions are about the same and are appreciably larger than the rotational fraction. However, above 50 kcal mol^{-1} the rotational fraction begins to dominate over the vibrational fraction as the vibrational energy becomes increasingly diverted to translational energy with increasing collision energy. Figure 12(b) shows the breakdown of the energy fractions into active and spectator components. It is quite clear that the active OH has the majority of product internal energy and this tendency increases dramatically above ~40 kcal mol^{-1} collision en-

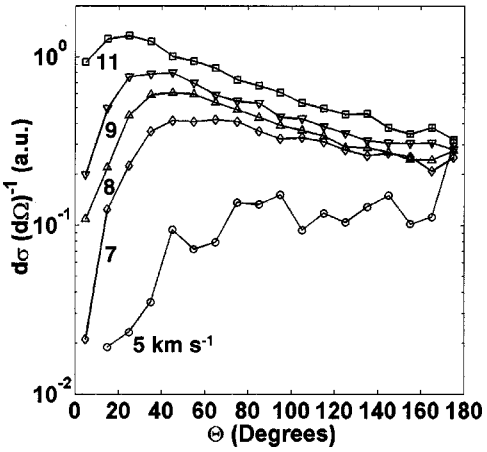

FIG. 13. Calculated differential angular cross sections as a function of collision velocity. ◯, results at 5 km s^{-1} collision velocity; ◇, results at 7 km s^{-1} collision velocity; △, results at 8 km s^{-1} collision velocity; ▽, results at 9 km s^{-1} collision velocity; □, results at 11 km s^{-1} collision velocity. To be consistent with previous results, we follow the convention for Eq. (16) for the total cross section.

TABLE IV. Relative populations of OD(v) and OH(v) for the measurements of Ref. 20 and for present results. Main entries are for HOD(4_vOH) and parentheses are for HOD(3_vOH).

	OD (Ref. 20)	OD (theory)	OH (Ref. 20)	OH (theory)
$v=0$	0.93±0.03	0.81 (0.90)	…	0.17 (0.25)
$v=1$	0.07±0.03	0.16 (0.10)	0.00±0.04	0.34 (0.41)
$v=2$	…	0.03 (0.00)	1.0±0.04	0.49 (0.34)

ergy. The largest changes with collision energy occur with the active and spectator vibrational energy fractions which decrease dramatically above 25 kcal mol^{-1} collision energy. As the collision energy increases, the vibrational energy fraction becomes diverted into rotation and translation, especially at the highest collision velocities.

4. Differential angular cross sections

The differential angular cross section summed over all OH states is shown in Fig. 13 at 5.0, 7.0, 8.0, 9.0, and 11.0 km s^{-1} collision velocity. At low collision velocities, the distribution is backward peaked, but as the collision velocity increases the angular distribution becomes more and more forward peaked, until at 11 km s^{-1} products are mostly forward scattered. There appears to be a change in mechanism from backward to forward peaked with collision velocity. This mirrors the changes in energy deposition from vibration to rotation and translation with collision energy, and indicates different reaction mechanisms at low and high energies. The changeover occurs between 5 and 7 km s^{-1}.

C. Comparisons to measurements of O(^3P) + HOD(X,4_vOH) → OH($X\,^2\Pi$) + OD($X\,^2\Pi$)

The same potential surfaces have been used to examine the measurements of Ref. 20 of the reaction O(^3P) + HOD(X,4_vOH) → OH($X\,^2\Pi$) + OD($X\,^2\Pi$). In these measurements, atomic oxygen formed from photolysis of NO_2 collides at collision energies of 1.69 kcal mol^{-1} with HOD in which the OH bond has been excited by four quanta. The necessary energy to create products is obtained mostly from excitation of the HOD reagent so that there is sufficient available energy (24.3 kcal mol^{-1}) to excite up to OD($v=3$) and OH($v=2$) products. Product internal energy distributions were probed with laser-induced fluorescence. Table IV shows the experimental and theoretical relative populations of OD(v) and OH(v). The theoretical results only use electronic state 1. Our classical trajectory approach generates harmonic initial HOD(v) states, so there is a ~5 kcal mol^{-1} energy surplus in the total energy due to neglect of anharmonicity. This extra energy was enough to populate OH($v=3$) states. Hence, we obtained theoretical results for the HOD(X,4_vOH) reagent, and also for HOD(X,3_vOH) reagent to partly correct for the surplus initial energy in the present classical calculations.

As described in Ref. 20, most of the initial vibrational energy in the OH bond of HOD is retained in the OH product, and the OD functions like a spectator in the reaction. For the HOD(X,4_vOH) reagent, the theoretical results agree well with the measured OD(v) populations, but there is only qualitative agreement with measurements for the OH(v) populations. The theoretical results are largest for OH($v=2$) but there is appreciable population in $v=0$ and $v=1$. For HOD(X,3_vOH), the spread of OH(v) products is much greater than experiment, with the OH($v=1$) level greatest.

Figure 14 shows the relative populations of OD($v=0,j$) and OH($v=2,j$) states, for the measurements of Ref. 20 and the present theoretical results. For HOD(4_vOH) reagents, there is fairly good agreement for OD($v=0,j$) populations but there is considerable disagreement for the OH($v=2,j$) populations. Because of the larger initial total energy and due to the histogram binning method used in the dynamics calculations (which include trajectories at edges of quantum bins), the theoretical results product OH($j>10$) states which correspond to total energies beyond the range of the experimental conditions. For the HOD(3_vOH) reagent where the total energy is a better match to the experimental conditions, there is much better agreement with measurements for OH($v=2,j$), and there is still good agreement for OD($v=0,j$). (We note that some of the oscillatory structure of the calculated rotational populations is due to statistical scatter.) If we employ a Gaussian binning method and retain only those trajectories near the center of quantum bins, preliminary calculations show that the higher energy OH($v=2,j>10$) populations diminish greatly and there is even better agreement with measurements. We also show in Fig. 14 the relative populations for OD($v=0,j$) and OH($v=2,j$) for a rotational temperature of 700 K which is fairly close to the temperature implied by the relative collision energy. The 700

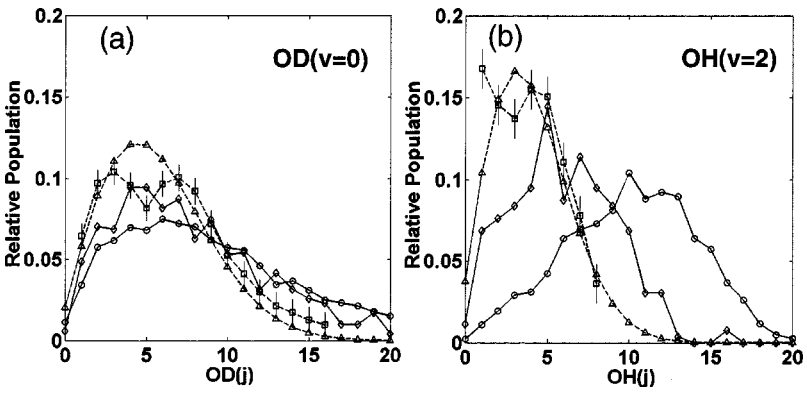

FIG. 14. Rotational relative populations for the reaction O(^3P) + HOD(4vOH) → OD(v,j) + OH(v,j). (a) Results for OD($v=0$) product: - -□- -, experimental results of Ref. 20; —◯—, present calculated results for HOD(4vOH); —◇—, present calculated results for HOD(3vOH); - -△- -, population of OD($v=0,j$) at 700 K. (b) Same as (a) except for OD($v=2,j$).

K temperature populations are a good fit to the data, and this could suggest that collisional relaxation plays a role in determining these populations.

IV. FUTURE WORK

The present calculated results for reaction (1) are well suited for planning and analyses of hyperthermal O-atom measurements[21] that should be possible in the near future. If final state resolution is possible, such measurements would be an ideal way to assess the accuracy of the present surfaces and dynamics results and explore the rich dynamics of this system. The present surfaces can also be used to investigate direct collisional excitation of $H_2O(X\,^1A_1)$ by $O(^3P)$, reaction (2). For further analysis of the laboratory and space-based spectral data, direct collisional excitation results will be critical. This is probably best carried out with quantum scattering approaches, as resolution of final quantum states for polyatomic systems, although done previously,[13] presents special problems with classical approaches. It is also possible to model $OH(X\,^2\Pi)+OH(X\,^2\Pi)$ collisions, the reverse of reaction (1), with the present surfaces, although the present surfaces only involve three of the four electronic states on the OH+OH side. Since $OH(X\,^2\Pi)+OH(X\,^2\Pi)$ collisions to make H_2O are exothermic, measurements of the reverse of Eq. (1) are more experimentally accessible. We should mention also that the present work does not consider singlet surfaces nor electronic or Coriolis coupling which could be important in comparing to detailed measurements. Finally, we note that the present surfaces form the lower part of a large electronic state manifold leading to electronically excited $OH(A\,^2\Sigma^+)$.[12] The present approaches and surfaces together with information from Ref. 12 could be used as the basis to construct global surfaces with couplings leading to electronically excited OH observed in several measurements.[10,11]

ACKNOWLEDGMENTS

The authors acknowledge support through a Small Business Innovative Research (SBIR) award from the Missile Defense Agency (MDA) under Contract No. F04611-03-C-0015, and technical oversight from Dr. Marty Venner of the Air Force Research Laboratory. They also acknowledge support from the DoD through Contract No. F19628-00-C-0006. This work has benefited greatly from discussions with George Schatz, Bisu Maiti, Timothy Minton, James Duff, and Steve Adler-Golden. They also acknowledge William Hase for making the VENUS trajectory code available to them.

[1] M. G. Dunn, G. T. Skinner, and C. E. Treanor, AIAA J. **13**, 803 (1975).
[2] C. E. Kolb and J. B. Elgin, J. Chem. Phys. **66**, 119 (1977).
[3] J. W. Duff, S. C. Richtsmeier, L. S. Bernstein, H. H. K. Burke, and M. Pietrzyk, J. Spacecr. Rockets **30**, 755 (1993).
[4] G. E. Caledonia, AIAA paper 00-0104 (2000), and as reported in Ref. 7.
[5] D. K. Zhou, W. R. Pendleton, Jr., G. E. Bingham, D. C. Thompson, W. J. Raitt, and R. M. Nadile, J. Geophys. Res. **99**, 19585 (1994).
[6] R. E. Meyerott, G. R. Swenson, E. L. Schweitzer, and D. G. Koch, J. Geophys. Res. **99**, 17559 (1994).
[7] L. S. Bernstein, J. B. Elgin, C. P. Pike, D. J. Knecht, E. E. Murad, T. F. Zehnpfennig, G. E. Galicia, and A. T. Stair, Jr., J. Geophys. Res. **101**, 383 (1996).
[8] D. P. Murtagh, E. J. Llewellyn, and P. J. Espy, Geophys. Res. Lett. **24**, 85 (1997).
[9] D. L. A Rall, I. L. Kofsky, C. P. Pike, D. J. Knecht, and T. P. Zehnpfennig, J. Spacecr. Rockets **33**, 393 (1996).
[10] O. J. Orient, A. Chutijan, and E. Murad, Phys. Rev. Lett. **65**, 2359 (1990).
[11] L. Bernstein, Y. Chiu, J. A. Gardner, A. L. Broadfoot, M. Lester, M. Tsiouris, R. Dressler, and E. Murad, J. Phys. Chem. **107**, 10695 (2003).
[12] S. Matsik and D. R. Yarkony, J. Chem. Phys. **117**, 3733 (2002).
[13] M. J. Redmon, G. C. Schatz, and B. C. Garrett, J. Chem. Phys. **84**, 764 (1986).
[14] B. R. Johnson, J. Chem. Phys. **84**, 176 (1986).
[15] R. J. Bartlett and M. J. Redmon, Report No. AFRL-TR-81-27 (unpublished).
[16] R. J. Redmon, R. J. Bartlett, B. C. Garrett, G. D. Purvis III, P. M. Saatzer, G. C. Schatz, and I. Shavitt, *Potential Energy Surfaces and Dynamics Calculations*, edited by D. G. Truhlar (Plenum, New York, 1981), pp. 771–803.
[17] S. P. Karkach and V. I. Osherov, J. Chem. Phys. **110**, 11918 (1999).
[18] D. W. Arnold, C. Xu, and D. M. Neumark, J. Chem. Phys. **102**, 6088 (1995).
[19] H.-J. Deyerl, T. G. Clements, A. K. Luong, and R. E. Continetti, J. Chem. Phys. **115**, 6931 (2001).
[20] J. M. Pfeiffer, E. Woods III, R. B. Metz, and F. Fleming Crim, J. Chem. Phys. **113**, 7982 (2000).
[21] D. J. Garton, T. K. Minton, D. Troya, R. Pascual, and G. C. Schatz, J. Phys. Chem. A **107**, 4583 (2003).
[22] W. Tsang and R. F. Hampson, J. Phys. Chem. Ref. Data **15**, 1087 (1986).
[23] A. Lifschitz and J. V. Michael, Symp. Int. Combust. Proc. **23**, 59 (1991).
[24] R. Sayos, C. Oliva, and M. Gonzalez, J. Chem. Phys. **115**, 8828 (2001).
[25] G. Wu, G. C. Schatz, G. Lendvay, D.-C. Fang, and L. B. Harding, J. Chem. Phys. **113**, 3150 (2000).
[26] D. McCune, Princeton Spline and Hermite Cubic Interpolation Routines, Princeton Plasma Physics Laboratory, http://w3.pppl.gov/NTCC/PSPLINE/ (2000).
[27] H. Partridge and D. W. Schwenke, J. Chem. Phys. **106**, 4618 (1997).
[28] K. P. Huber and G. Herzberg, *Constants of Diatomic Molecules* (Van Nostrand, Princeton, 1979).
[29] M. W. Schmidt, K. K. Baldridge, J. A. Boatz *et al.*, J. Comput. Chem. **14**, 1347 (1993).
[30] L. Harding, J. Phys. Chem. **95**, 8653 (1991).
[31] VENUS96: A General Chemical Dynamics Program, Program 671, The William L. Hase Research Group, Quantum Chemistry Program Exchange, http://qcpe.chem.indiana.edu/.
[32] R. D. Levine and R. B. Bernstein, *Molecular Reaction Dynamics and Chemical Reactivity* (Oxford University Press, Oxford, 1987), Chap. 5.